Earth and Planetary Science Letters 602 (2023) 117958

Contents lists available at ScienceDirect

Earth and Planetary Science Letters

journal homepage: www.elsevier.com/locate/epsl

Trace element evidence for serial processing of the lunar flotation crust and a depleted bulk Moon

Dian Ji, Nicholas Dygert *

Department of Earth and Planetary Sciences, University of Tennessee, Knoxville, TN 37996, United States of America

ARTICLE INFO

Article history:
Received 22 September 2022
Received in revised form 28 November 2022
Accepted 7 December 2022
Available online 29 December 2022
Editor: F. Moynier

Keywords:
lunar anorthosite
magma ocean
subsolidus reequilibration
differentiation

ABSTRACT

Plagioclase in lunar anorthositic crust have rare earth element (REE) patterns and Eu abundances which cannot be directly produced by lunar magma ocean (LMO) solidification. This is surprising as the LMO is invoked to explain the mineralogy of the crust, and other lunar surface and interior properties. We explored geological processes subsequent to LMO solidification that could reconcile anorthositic compositions with an LMO, finding that subsolidus reequilibration after addition of a minor KREEPy component successfully reproduces REE variations in natural samples. Monte-Carlo simulations used to constrain conditions of subsolidus reequilibration suggest the Moon has a light-REE depleted bulk composition. We propose a post-LMO serial processing model to reconcile the petrological, geochronological, and isotopic characteristics of lunar anorthosites and contemporaneous magmatism. If the bulk Earth is chondritic and the Moon accreted from material ejected from a depleted terrestrial reservoir, Earth underwent an early differentiation event prior to the Moon-forming giant impact.

1. Introduction

In seminal studies of Apollo 11 samples, researchers found ubiquitous anorthositic lithologies and put forward the hypothesis of the lunar magma ocean (LMO; e.g., Binder, 1974). The model argues that the Moon underwent global melting, producing a magma ocean and that as the magma ocean solidified, relatively low-density anorthosites segregated at the surface because of their buoyancy. The formation of the lunar highland crust by LMO solidification would be accompanied by formation of complementary mafic cumulate layers in the lunar interior (Snyder et al., 1992a). Recently, researchers ran experiments that constrain the mineralogy and mineral compositions of LMO cumulates for different bulk LMO compositions (Fig. S1; Charlier et al., 2018; Lin et al., 2017; Rapp and Draper, 2018; Schmidt and Kraettli, 2022). Here, we use experimentally determined crystallization sequences to explore trace element fractionation during LMO solidification for different staring bulk compositions. Leveraging the experimental data and mineral-melt REE partitioning models, we calculate the predicted REE patterns of minerals in lunar anorthosites and compare the results to natural samples to evaluate their petrogenesis.

Our work is motivated by disagreement about the formation of lunar anorthosites (e.g., Gross and Joy, 2016). Some researchers argue the ferroan anorthosites are not a direct product of the LMO but formed from partial melting of the early mafic cumulates after LMO solidification, during gravitational restructuring of the Moon (e.g., Longhi, 2003). Arai et al. (2008) argued for an LMO origin, but suggested that asymmetric crystallization of the LMO caused by a surface convectional force related to the shielding effect of the Earth, affected the formation of anorthositic crust in a hemispheric way, leading to crystallization of the higher-Mg# anorthosite on the farside before crystallization of lower Mg# anorthosites on the nearside. Other researchers argued that after LMO solidification, melts derived from decompression melting of ultramafic cumulates in the deep lunar interior would interact with crystallized anorthosites, which can explain the similarities in the geochemical, mineralogical and age characteristics of lunar anorthosites and the intrusive Mg-suite (Dygert et al., 2017; Pernet-Fisher et al., 2019). Haskin et al. (1981) proposed that partial melting of anorthosites with the addition of a small amount of trapped liquid can help to explain their REE patterns. Others highlight the role of trapped magma ocean liquid that may have been frozen in the anorthosites as they floated on the LMO (e.g., Raedeke and McCallum, 1980; Piskorz and Stevenson, 2014).

To assess the formation of the lunar anorthosites in an LMO and their subsequent modification in the context of the aforementioned models, we compared the geochemical characteristics of plagioclase calculated from different LMO solidification scenarios with

* Corresponding author at: Department of Earth and Planetary Sciences, University of Tennessee, Knoxville, 1621 Cumberland Avenue, 602 Strong Hall, Knoxville, TN 37996, United States of America.
E-mail address: ndygert1@utk.edu (N. Dygert).

https://doi.org/10.1016/j.epsl.2022.117958
0012-821X/

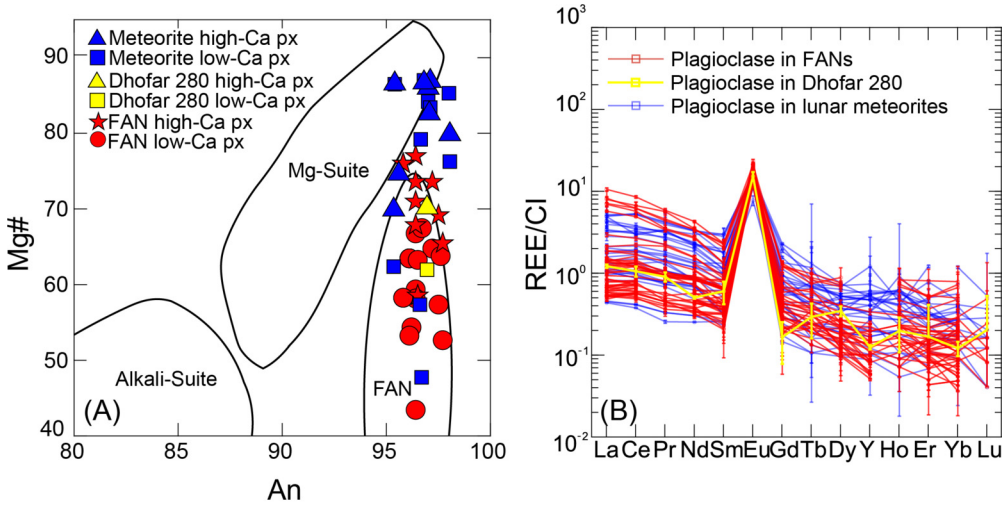

Fig. 1. Major and trace elements in minerals from Apollo FANs and lunar anorthositic meteorites. (**A**) Mg# (100 × molar Mg/[Mg + Fe]) in pyroxenes (y-axis) versus An (100 × molar Ca/[Ca + Na + K] or 100 × molar Ca/[Ca + Na]) in coexisting plagioclase (x-axis). Fields of Alkali Suite, Mg-suite and FAN are from (Roberts et al., 2019). (**B**) Chondrite-normalized REE patterns for plagioclase in lunar FANs and meteorites (Table S3). Yellow line shows new data for Dhofar 280. Chondrite normalization is from Lodders (2021). Data sources are Cahill et al. (2004), Floss et al. (1998), Gross et al. (2014), McGee (1993), Papike et al. (1997), Pernet-Fisher et al. (2019), Roberts et al. (2019), Russell et al. (2014), Treiman et al. (2010), and this study (Table S2). (For interpretation of the colors in the figure(s), the reader is referred to the web version of this article.)

Apollo samples and lunar anorthositic meteorites. Specifically, we focus on Eu anomalies (Eu/Eu*, where Eu is the chondrite normalized abundance and Eu* is the interpolated value from neighboring elements on a REE diagram) and the slope of REE patterns of plagioclase and test the consequences of partial melting, subsolidus reequilibration, and addition of chondritic, trapped LMO liquid, and KREEPy components on the compositions of the anorthosites. We evaluate the effects of these processes for LMOs with differing bulk major and trace element compositions. Finally, we evaluate the physical and chemical conditions under which the anorthosites formed and evolved using Monte-Carlo simulations that place constraints on the bulk LMO composition.

2. Compositional characteristics of samples used for comparison to our models

As the major rock type of the lunar crust, highland anorthosites are composed of calcic plagioclase (usually >90 vol %; Table S1 and Fig. S2) with a small amount of pyroxene (orthopyroxene and/or pigeonite, which we refer to here and elsewhere as low-Ca pyroxene, and augite or clinopyroxene, which we refer to as high-Ca pyroxene). Some anorthosites also contain minor olivines (e.g., 62236 and 62237), and other accessory phases (e.g., ilmenite, chromite, troilite, (Zn,Fe)S, and FeNi metal, McGee, 1993; but not phosphates, Norman et al., 2003). We compiled plagioclase compositions from Apollo ferroan anorthosite (FAN) samples and lunar anorthositic meteorites (Cahill et al., 2004; Floss et al., 1998; Gross et al., 2014; McGee, 1993; Papike et al., 1997; Pernet-Fisher et al., 2019; Roberts et al., 2019; Russell et al., 2014; Treiman et al., 2010), and augmented the literature data with new analyses of lunar meteorite Dhofar 280 (an anorthositic fragmental breccia, see description in the Supplementary Materials, and analytical results in Table S2). Concentrations of REEs in plagioclase in the samples we investigate here, and their associated uncertainties, are summarized in Table S3. We include as much data as possible in our compilation, including anorthosites reported not to exhibit metamorphic texture (i.e., granulitic texture; McGee, 1993). An example is 60025, which been proposed to have undergone subsolidus reequilibration based on trace element distributions and age determinations (Torcivia and Neal, 2022). We note that some researchers divided FAN into petrological and geochemical subgroups (e.g., Floss et al., 1998; McGee, 1994), which were interpreted to reflect different petrogenetic histories. Here, we choose not to subdivide FANs because we conclude their ubiquitous REE patterns may be suggestive of a global post-formation process. However, we do not consider samples with plagioclase that display high shock states (e.g., 60015,125 in Pernet-Fisher et al., 2019) or those missing REE data required for modeling.

In general, the plagioclase in both Apollo FANs and lunar anorthositic meteorites show high An#s (94.8 – 98.0, where the An# = 100 × molar Ca/[Ca + Na + K], or An# = 100 × molar Ca/[Ca + Na] where K is not reported), while the coexisting pyroxenes in lunar anorthositic meteorites are more magnesian (Fig. 1A; e.g., Gross et al., 2014). Plagioclase show no linear relationship in major elements with coexisting pyroxenes, which is thought to be the result of trapped intercumulus liquid crystallization (e.g., Raedeke and McCallum, 1980) and/or evolution after secondary processing (McGee, 1993; Phinney, 1992). The REE patterns of plagioclase in both lunar anorthositic meteorites and Apollo FANs show variable slopes [$(La/Yb)_{CI}$ = 2 - 32], with positive but variable Eu anomalies (6 – 81; Fig. 1B). A detailed description of the geochemical characteristics of plagioclase we compiled is included in the Supplementary Materials.

3. Lunar magma ocean crystallization modeling

Researchers have studied the implications of LMO crystallization for decades (e.g., Longhi, 1978; Snyder et al., 1992a). However, in early investigations of LMO solidification, knowledge of the bulk LMO composition and phase equilibria constraints on magma ocean cumulates were limited. More recently, three laboratories experimentally determined crystallization sequences for LMOs with different bulk compositions (Fig. S1; Charlier et al., 2018; Lin et al., 2017; Rapp and Draper, 2018). These models improve upon the widely cited Snyder et al. (1992a) study, by experimentally simulating complete polybaric solidification of the LMO for lunar bulk compositions consistent with modern crustal thickness estimates (e.g., Taylor and Wieczorek, 2014).

In the experiments, the residual magma ocean liquids reached plagioclase saturation at different percent solidification (PCS), and were cosaturated with different phases depending on the bulk compositions assumed. Lin et al. (2017) assumed a bulk LMO sim-

ilar to Bulk Silicate Earth (McDonough and Sun, 1995), observing plagioclase saturation at 68 PCS, with olivine and high-Ca pyroxenes. Rapp and Draper (2018) utilized a Lunar Primitive Upper Mantle (Longhi, 2006) bulk LMO composition and observed plagioclase at 74 PCS with olivine, low-Ca pyroxenes and high-Ca pyroxenes. Charlier et al. (2018) tested three different bulk compositions: O'Neill (O'Neill, 1991), the Taylor Whole Moon (TWM; Taylor, 1982) and the Lunar Primitive Upper Mantle (LPUM) model (Longhi, 2006), which produced plagioclase at 78 PCS with high-Ca pyroxenes and low-Ca pyroxenes, 67 PCS with low-Ca pyroxenes, and 81 PCS with high-Ca pyroxenes and low-Ca pyroxenes, respectively. We note the more aluminous TWM model is untenable in the context of lunar gravimetric data, which suggests a relatively thin crust (40 km on average, Wieczorek et al., 2013). Nonetheless, we used all five crystallization sequences from the aforementioned studies to calculate elemental distributions in the magma ocean cumulates, including the lunar anorthosites. A most recent experimental lunar magma ocean solidification study by Schmidt and Kraettli (2022) recovered results comparable to the previous LMO crystallization experiments, and assumed a TWM bulk composition.

In previous work, researchers assumed a chondritic REE pattern as representing the initial bulk Moon (e.g., Rapp and Draper, 2018; Snyder et al., 1992a). However, given that abundant isotopic evidence suggests the initial bulk composition of the Moon may be closely related to the proto-Earth (e.g., Melosh, 2014, and references therein), we explored four distinct terrestrial trace element reservoirs as proxies for potential lunar bulk REE patterns (Table S4). These terrestrial reservoirs have different degrees of light-REE (LREE) enrichment or depletion and were diluted such that the average concentrations are consistent with CI chondrite. A LREE enriched Moon is represented by average continental crust from Earth (Rudnick and Gao, 2014, diluted by a factor of 20). A chondritic Moon is represented by the CI chondrite composition of Lodders (2021). A slightly LREE depleted Moon is represented by a log-normal mean global MORB pattern (Arevalo and McDonough, 2010, diluted by a factor of 20), and a moderately depleted Moon is represented by the depleted MORB mantle (or DMM) of Workman and Hart (2005), diluted by a factor of 2. These chondrite normalized REE patterns are plotted in Fig. 2A. Exploration of variably depleted bulk Moon compositions is justified by isotopic similarities between the Moon and Earth, and the ^{142}Nd system, which suggests that ancient lunar and terrestrial reservoirs have superchondritic Sm/Nd (e.g., Borg et al., 1999; Boyet and Carlson, 2007), or formed from precursor materials with nucleosynthetically anomalous ^{142}Nd (Boyet et al., 2015). Using experimentally parameterized partition coefficient models for equilibrium between silicate melt and olivine (Sun and Liang, 2013a), low-Ca pyroxene (Sun and Liang, 2013b), high-Ca pyroxene (Dygert et al., 2014), plagioclase (Sun et al., 2017), and ilmenite (Dygert et al., 2013), we calculated trivalent REE abundances in minerals in each part of the LMO crystallization sequence for the different bulk Moon major and trace element compositions.

The middle REE Eu can be divalent or trivalent depending on oxygen fugacity (fO_2), strongly affecting its partitioning behavior. Previous research demonstrates that at fO_2 below the iron-wüstite (IW) buffer, as in a reduced Moon, much of the Eu in geologic systems is divalent, and its substitution is favored in plagioclase because Eu^{2+} has an ionic radius similar to Ca^{2+}. Dygert et al. (2020) developed a model which enables us to predict Eu partitioning as a function of fO_2, T and plagioclase composition. The new Eu-in-plagioclase model is employed along with the aforementioned models to calculate elemental fractionation of the full suite of REEs during LMO solidification. In simulations shown in the main text, we assume trivalent Eu partitioning in pyroxene, as preliminary fO_2-dependent Eu partitioning models for pyroxenes

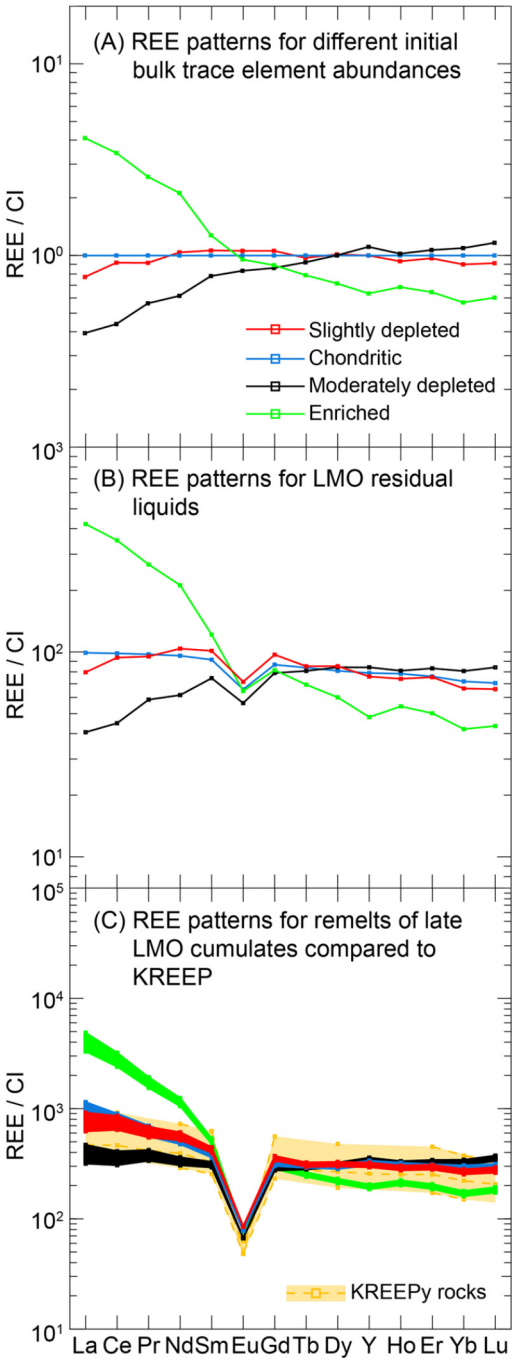

Fig. 2. Different initial bulk LMO trace element compositions and consequences for fractionation during and after LMO solidification. (**A**) Chondrite-normalized REE patterns tested as possible bulk Moon trace element compositions (Table S4), (**B**) residual liquids after 99 percent solidification of the LMO, and (**C**) remelts of late LMO cumulates compared to KREEPy rocks (KREEP basalt 15386, KREEP breccia 15405 and high-K KREEP; Neal and Kramer, 2003; Nyquist et al., 1976; Warren, 1989). In Fig. 2B, the $(Sm/Nd)_{CI}$ of LMO residual liquid with a slightly depleted, chondritic, moderately depleted and enriched initial bulk composition are 0.99, 0.97, 1.23 and 0.58, respectively. A $(Sm/Nd)_{CI} > 1$ (as in the moderately depleted case) may be inconsistent with Nd isotopic compositions of lunar materials. Fig. 2C shows compositions of remelts of late LMO cumulates assuming a source with 57% high-Ca pyroxene + 40% plagioclase + 1% apatite + 2% ilmenite. Since the apatite/melt partition coefficients for the REEs are closely related to melt polymerization, we choose partition coefficients of experiment 59B in (Prowatke and Klemme, 2006), that has the most similar silicate concentration of the melt with the 99 PCS residual liquid in Charlier et al. (2018). Due to the lack of published partition coefficients for Eu between apatite and melt, we use the D_{Sr} as a proxy for Eu. Here we show 1-4% instantaneous fractional modal melts. Melts of late LMO cumulates with a slightly depleted and chondritic initial bulk composition reproduce KREEPy REE patterns. Chondrite normalization is from Lodders (2021).

(Fabbrizio et al., 2021) produced results consistent with the trivalent Eu assumption for pyroxene (see Supplementary Fig. S11 for more details). We do not consider tetravalent Ce here since Ce^{4+} cannot be stabilized under lunar fO_2s (Snyder et al., 1992b).

Elemental concentrations in melt from each crystallization sequence were calculated via the Rayleigh fractionation equation:

$$C_L^i = C_{Lo}^i \times F^{(D_{Bulk}^i - 1)} \quad (1)$$

where C_L^i is the concentration of element i in melt, C_{Lo}^i is the concentration of element i in the initial bulk LMO, F is the degree of melt, and D_{Bulk}^i is the bulk partition coefficient calculated by the weighted average partition coefficient between mineral and melt based on mineral modes. We note that in fractional crystallization, when crystallizing phases change, D_{Bulk}^i must account for contributions of phases during preceding parts of the solidification sequence to ensure mass conservation. The concentration of element i in each mineral is:

$$C_s^i = C_L^i \times D_s^i \quad (2)$$

where C_s^i is the concentration of element i the mineral, and D_s^i is the partition coefficient of element i between the mineral and melt.

4. Eu anomalies in lunar plagioclase

Using Equations (1) and (2), we calculate the REE concentrations in plagioclase crystallized from different bulk LMOs for the different solidification models, as a function of fO_2. We test three fO_2 conditions, two orders of magnitude below the iron-wüstite buffer (IW-2), along the fayalite-magnetite-quartz buffer (FMQ), and two log units more oxidizing than the FMQ buffer. The most reducing condition (IW-2) is most lunar relevant (e.g., Rutherford et al., 2017). To develop a threshold for evaluating successful numerical simulations, we estimated the uncertainty of Eu* and $(Ce/Sm)_{CI}$ calculated by a Taylor series expansion in the chondritic normalization and the analyses of elemental concentrations in lunar plagioclase crystals using Eqs. (3) and (4) (e.g., Barford, 1985):

$$s_{Eu*} = \left(\left(\frac{\partial Eu*}{\partial Eu}\right)^2 s_{Eu}^2 + \left(\frac{\partial Eu*}{\partial Eu_{CI}}\right) s_{Eu_{CI}}^2 + \left(\frac{\partial Eu*}{\partial Sm}\right)^2 s_{Sm}^2 + \left(\frac{\partial Eu*}{\partial Sm_{CI}}\right) s_{Sm_{CI}}^2 + \left(\frac{\partial Eu*}{\partial Gd}\right)^2 s_{Gd}^2 + \left(\frac{\partial Eu*}{\partial Gd_{CI}}\right) s_{Gd_{CI}}^2\right)^{1/2} \quad (3)$$

$$s_{(Ce/Sm)_{CI}} = \left(\left(\frac{\partial (Ce/Sm)_{CI}}{\partial Ce}\right)^2 s_{Ce}^2 + \left(\frac{\partial (Ce/Sm)_{CI}}{\partial Ce_{CI}}\right) s_{Ce_{CI}}^2 + \left(\frac{\partial (Ce/Sm)_{CI}}{\partial Sm}\right)^2 s_{Sm}^2 + \left(\frac{\partial (Ce/Sm)_{CI}}{\partial Sm_{CI}}\right) s_{Sm_{CI}}^2\right)^{1/2} \quad (4)$$

where s_{Eu*} and $s_{(Ce/Sm)_{CI}}$ represent the errors (1σ) of Eu* and $(Ce/Sm)_{CI}$, S_{Eu} represents the error of Eu in plagioclase (Table S3), $S_{Eu_{CI}}$ represents the error of Eu in CI chondrites (Lodders, 2021), and so forth. $\frac{\partial Eu*}{\partial Eu}$ denotes the partial derivative of Eu* with respect to the Eu, $\frac{\partial (Ce/Sm)_{CI}}{\partial Ce}$ denotes the partial derivative of $(Ce/Sm)_{CI}$ with respect to the Ce, and so forth. For plagioclase in FANs and lunar anorthositic meteorites, the average percent error for $(Ce/Sm)_{CI}$ are 21.82% and 17.38%, while for Eu* are 17% and 14.3%, respectively (1σ). See Table S3 for sample-specific results of this error analysis.

In terms of Eu anomalies and in the slope of REE patterns, no matter which solidification sequence and trace element bulk composition combination we choose, the calculated plagioclase are inconsistent with many natural plagioclase from Apollo anorthosites and lunar anorthositic meteorites, even considering error propagation (Fig. 3A; Figs. S4 and S5). This is especially true for plagioclase produced in lunar-relevant low fO_2 scenarios, as the calculated plagioclase have larger Eu anomalies (163 to 355 in Fig. 4A) than the overwhelming majority of the natural samples (6.06 ± 1.10 to 79.91 ± 6.10; Table S3).

4.1. Partial melting of the lunar cumulates

After failure of LMO solidification alone to match the Eu/Eu* and $(Ce/Sm)_{CI}$ of the lunar anorthosites, we considered partial melting of LMO flotation cumulates as a potential secondary process for affecting their trace element compositions (e.g., Longhi, 2003). We chose cumulates from LMO solidification models with modes of 95.1% plagioclase and 4.9% pyroxenes (Warren, 1990). We explored scenarios that assume all pyroxene is low-Ca pyroxene and others where all pyroxene is high-Ca pyroxene. We simplify the partial melting as non-modal fractional melting to calculate the concentrations of elements in the fractional liquid:

$$C_L^i = \frac{C_o^i}{D_{bulk}^i} \times \left(1 - \frac{P_{bulk}^i * F}{D_{bulk}^i}\right)^{\left(\frac{1}{D_{Bulk}^i - 1}\right)} \quad (5)$$

where C_L^i is the concentration of element i in the liquid, C_o^i is the initial concentration of element i in the anorthositic melting residue, F is the degree of melting, D_{Bulk}^i is the bulk partition coefficient of anorthosites calculated by the weighted average of partition coefficient between mineral and liquid based on mineral modes, and P_{Bulk}^i is the non-modal contribution of each phase in the melting reaction, where we assume 58% low-Ca pyroxene and 42% plagioclase. Using the relationship for equilibrium partitioning (Eq. (2)), we obtain the concentration of element i in plagioclase in equilibrium with the melt.

In Fig. 3B, we show the result of a representative simulation based on the solidification sequence of all experiments with slightly LREE depleted initial bulk LMO composition, because the trend of results from all solidification models and bulk trace element compositions are similar and all of the results failed to reproduce most plagioclase (Figs. S6 and S7). After partial melting, we find that the slope of the REE patterns $(Ce/Sm)_{CI}$ of plagioclase in equilibrium with melts change, but the Eu anomalies become larger, opposite the direction needed to match the natural samples. It is apparent that partial melting exacerbates the Eu anomaly discrepancy, which is contrary to the trend of plagioclase in Apollo and anorthositic meteorite samples.

Haskin et al. (1981) proposed that adding a few percent of trapped liquid into the anorthosites can help explain the REE pattern variation after partial melting. Considering the amount of tapped LMO liquid fraction in the anorthosite cannot be greater than a few percent (Dygert et al., 2017; Krättli and Schmidt, 2021), we explored adding 4% of trapped LMO liquid and it indeed helped to reduce the Eu anomalies and increase the $(Ce/Sm)_{CI}$, but the effect is too limited to explain most of the plagioclase (Fig. 4B, partially transparent stars).

4.2. Subsolidus reequilibration

As reported by McGee (1993), some lunar anorthosites (e.g., 67525, 67535, 67536 and 68515) show clearly granulitic texture that may be related to subsolidus reequilibration, which is also

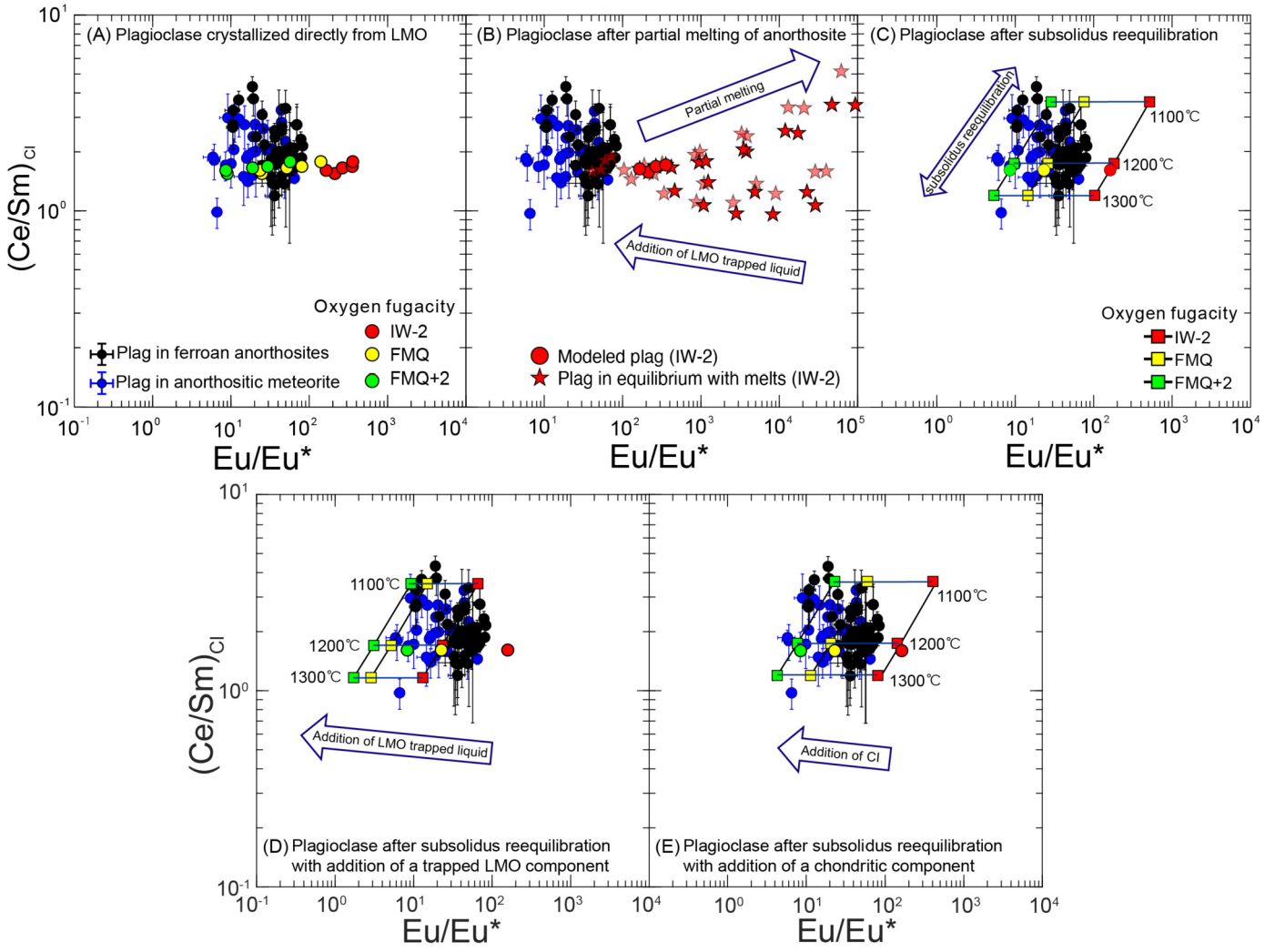

Fig. 3. Plagioclase produced by LMO solidification compared to returned Apollo ferroan anorthosites and lunar anorthositic meteorites (**A**), and a series of secondary process that could be invoked to explain the elemental variations exhibited by the natural lunar samples, which are all unsuccessful (**B**)-(**E**). (**A**) Modeled plagioclase compositions after LMO solidification as a function of fO_2 (colored circles) compared to lunar plagioclase in Apollo FANs (black circles) and lunar anorthositic meteorites (blue circles; Table S3). Y axis shows chondrite-normalized Ce/Sm, x axis shows Eu/Eu*. (**B**) Plagioclase in equilibrium with melts from partial melting of the calculated anorthositic lunar crust (red stars; fO_2 = IW-2). Simulations assuming addition of 4% trapped LMO liquid are shown by the partially transparent stars. (**C**) Modeled plagioclase before (colored circles) and after subsolidus reequilibration (colored squares). (**D**) Modeled plagioclase after subsolidus reequilibration with the addition of 8% trapped LMO liquid, and (**E**) after addition of 8% (by mass) of a chondritic component. As lunar-relevant fO_2s likely approximate IW-2, none of these mechanisms successfully explain the elemental distributions of all samples even considering the propagation of errors. In all simulations shown, we assume the mineral mode of anorthosite is 95.1% plagioclase + 4.9% low-Ca pyroxene. The simulations show representative results based on the solidification sequence from Charlier et al. (2018), assuming an LMO with an LPUM bulk major element composition. The trace element composition of the bulk LMO assumed is slightly depleted (Arevalo and McDonough, 2010). Because plagioclase crystallizes in multiple experimental stages in each LMO solidification sequence, the plagioclase shown in (**C**), (**D**) and (**E**) are those crystallized from the relatively early stage (82 percent solidification). The error bars are calculated considering error propagation (Table S3).

suggested by the concentrations and nonlinear relationship between FeO, MgO and An in plagioclase from lunar anorthosites (McGee, 1993; Phinney, 1992; Fig. S3). Subsolidus reequilibration may redistribute elements among minerals in a closed system after crystallization, perturbing elemental distributions from those initially representing high-T magmatic processes (Sun and Liang, 2014). We evaluated T-dependent subsolidus reequilibration assuming a closed system composed of plagioclase and minor amounts of pyroxenes that are initially in equilibrium with coexisting residual LMO liquid (e.g., Pernet-Fisher et al., 2017). Assuming subsequent segregation from the magma ocean, we treat the cumulates as a new closed system with a fixed mineral composition (95.1% plagioclase + 4.9% low-Ca pyroxene; Warren, 1990). We calculate the concentration of elements in this closed system:

$$C_{Bulk}^{Subsolidus} = \phi_{plag} \times C_{plag}^{Magmatic} + \phi_{opx} \times C_{opx}^{Magmatic} \quad (6)$$

where $C_{Bulk}^{Subsolidus}$ is the bulk concentration, $C_{plag}^{Magmatic}$ and $C_{opx}^{Magmatic}$ are the concentrations of elements in crystallized plagioclase and low-Ca pyroxenes from LMO cumulates, and ϕ_{plag} and ϕ_{opx} are the mass proportions of the two minerals in the system, which we approximate here by volume proportions. In order to evaluate the redistribution of elements under subsolidus conditions, mineral-melt partition coefficients must be recalculated as mineral-mineral partition coefficients, e.g.,:

$$\frac{D_{opx-melt}(\mathrm{T}, X)}{D_{plag-melt}(fO_2, \mathrm{T}, X)} = D_{opx-plag}(fO_2, \mathrm{T}, X) \quad (7)$$

where $D_{plag-melt}$ is the partition coefficient of elements between the plagioclase and melt, $D_{opx-melt}$ is the partition coefficient of elements between the low-Ca pyroxenes and melt, $D_{plag-opx}$ is the partition coefficient of elements between plagioclase and low-Ca pyroxenes. $D_{plag-opx}$ is temperature (T), composition (X) and fO_2

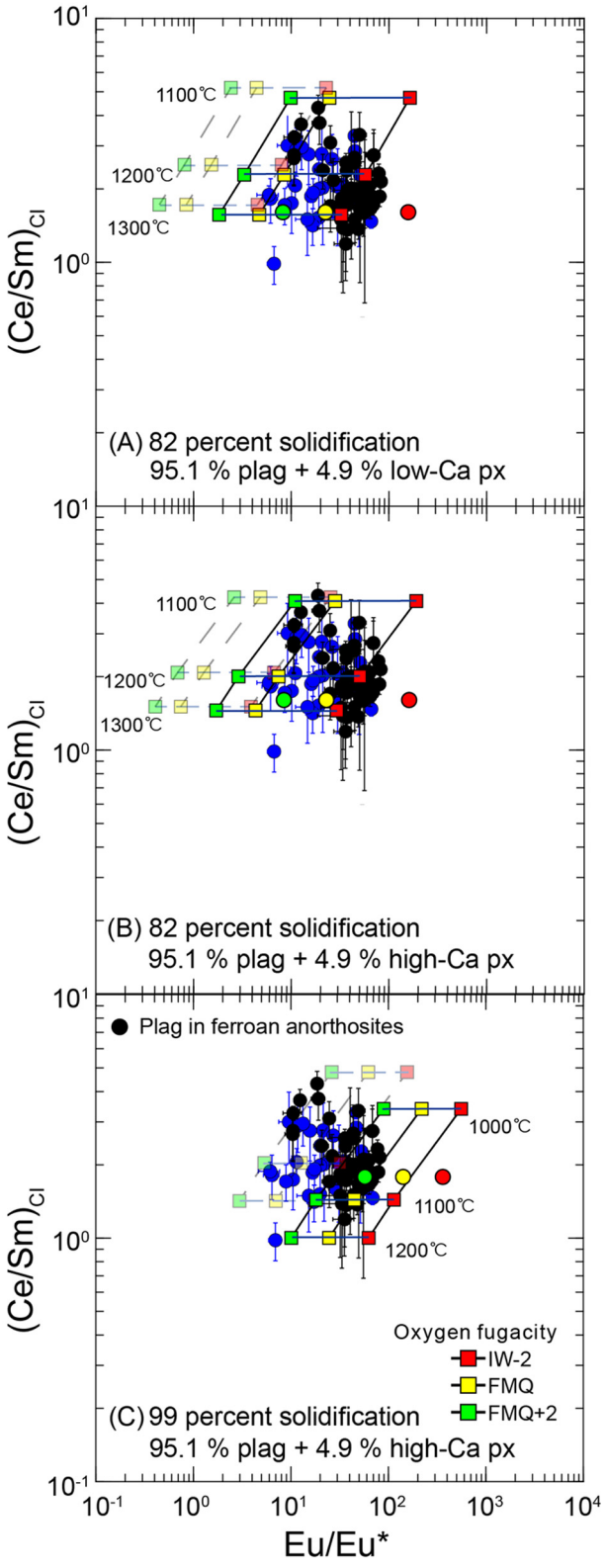

Fig. 4. Figures illustrating that subsolidus reequilibration of plagioclase crystals produced by LMO solidification after addition of a KREEPy component successfully reproduces compositions of Apollo FANs and lunar anorthositic meteorites. Panels (**A**) and (**B**) compare models assuming subsolidus reequilibration with low- and high-Ca pyroxene when LMO solidification is 82 percent, while panel (**C**) shows subsolidus reequilibration with high-Ca pyroxene when LMO solidification is 99 percent. Simulations assuming addition of 0.25% KREEPy component are shown by opaque symbols and solid lines and simulations assuming addition of 2.5% KREEPy component are shown by the partially transparent symbols and dashed lines. Modeling conditions are otherwise as described in the caption to Fig. 3.

dependent. Then with assumed mineral modes and calculated REE concentrations in the system ($C_{Bulk}^{Subsolidus}$), we calculate REE concentrations in plagioclase under different T and fO_2 via a mass balance equation:

$$C_{plag}^{Subsolidus} = \frac{C_{Bulk}^{Subsolidus}}{\phi_{cpx} \times D_{opx-plag} + \phi_{plag}} \quad (8)$$

where $C_{plag}^{Subsolidus}$ is the concentration of elements in plagioclase after subsolidus reequilibration.

Here we show representative results based on the LPUM LMO solidification sequence from Charlier et al. (2018), assuming slightly depleted initial bulk trace element composition. We investigate plagioclase formed in the early stage of plagioclase precipitation from the LMO (82 PCS) as these cumulates would be located in the outmost layer of the Moon and are most likely to be sampled. We find that T-dependent closed-system subsolidus reequilibration expands the possible range of $(Ce/Sm)_{CI}$ as well as Eu anomalies in plagioclase (Fig. 3C). Subsolidus reequilibration under different fO_2s affects the Eu anomalies, while T affects the Eu anomalies as well as the slope of REE patterns. The lower the T and fO_2, the more Eu tends to enter plagioclase after reequilibration. However, the variation of Eu anomalies is still limited and cannot fit many natural samples under fO_2 conditions relevant to a reduced Moon.

4.3. Subsolidus reequilibration with minor trapped LMO liquid or a chondritic component

The potential importance of interstitial trapped liquid in the petrogenesis of anorthosites has been noted in many studies (e.g., Jolliff and Haskin, 1995; Piskorz and Stevenson, 2014; Raedeke and McCallum, 1980). To explore its effect on the elemental variations, here we added an ~8% of trapped residual LMO liquid component to our closed system. We calculated the compositions of trapped liquid based on assumed LMO crystallization sequences for each initial bulk LMO assumed and PCS. We observe that even under different fO_2 conditions, if as much as 8% modal LMO liquid was added, the Eu anomaly magnitude and slope of REE patterns are reduced, but plagioclase with lower $(Ce/Sm)_{CI}$ and higher Eu anomalies are not reproduced (Fig. 3D). As we mentioned earlier, in any case, research on the compaction of trapped liquids in plagioclase-melt mushes suggests contribution of so much trapped liquid to the closed system is implausible (e.g., Dygert et al., 2017; Krättli and Schmidt, 2021). A similar but weaker trend appears when we assume the addition of a chondritic meteoritic component to our closed system (Fig. 3E).

4.4. Subsolidus reequilibration with addition of a minor KREEPy component

Finally, we explored subsolidus reequilibration after addition of a KREEPy component (Fig. 4). The KREEPy component we choose in this study is KREEP basalt 15386 (Table S4; Neal and Kramer, 2003) that has a high REE concentration and an enrichment in LREEs compared with HREEs, with a strongly negative Eu anomaly (Fig. 2C). Addition of minor KREEPy component reduces Eu anomalies and elevates Ce/Sm ratios, reproducing variations in the natural samples. The proportion of KREEPy component required depends on the bulk LMO composition assumed. The more KREEPy component is added, the more the Eu anomaly decreases and the greater the slope of REE patterns. In general, compared to Apollo anorthosites, plagioclase in lunar anorthositic meteorites have less pronounced Eu anomalies (e.g., Fig. 4), requiring reequilibration at a higher temperature and/or addition of more KREEPy component.

4.5. The effect of pyroxene species and LMO solidification

Our compilation of reported Apollo anorthosite mineral modes (Table S1) reveals that in most cases, anorthosites contain both high-Ca pyroxenes and low-Ca pyroxenes, and high-Ca pyroxenes are even dominant in some samples (e.g., 15362, 15415 and 60055). Our previous calculations are based on the assumption that all pyroxenes are low-Ca pyroxenes, so it is necessary to evaluate how different kinds of pyroxenes would affect the Eu anomalies in plagioclase after reequilibration. We calculate the partition coefficient for low-Ca and high-Ca pyroxene crystallized in the same PCS in Charlier et al. (2018), and find under different temperatures and fO_2, the effect of reequilibration on the slope of REE patterns and Eu anomalies when high-Ca pyroxenes are dominant in pyroxenes is very similar to the previous result (compare Figs. 4A and 4B). Thus, subsolidus reequilibration after addition of a KREEPy component can explain most of the natural samples, regardless of the pyroxene type.

We note that with the solidification of the LMO (increasing PCS), the liquid in equilibrium with both plagioclase and pyroxene is progressively enriched, as are the minerals. Therefore, we need to add more KREEPy component and assume a lower temperature during subsolidus reequilibration in order to explain those plagioclase with higher $(Ce/Sm)_{CI}$ and lower Eu anomalies (compare Figs. 4B and 4C).

4.6. Feasibility of subsolidus reequilibration

Diffusive redistribution of elements among minerals in geologic systems may be restricted by exchange kinetics. To test the feasibility of subsolidus reequilibration under lunar crustal conditions, we calculated characteristic diffusion timescales for REEs in plagioclase and pyroxene:

$$t = \frac{L^2}{D_o exp\left(\frac{-E}{RT}\right)} \tag{9}$$

where t is the time for diffusive interaction, E and D_o are the activation energy and pre-exponential factors for Arrhenius models of diffusivity, respectively, R is the gas constant, T is the temperature for elemental redistribution, and L is the effective diffusion length of minerals experiencing reequilibration. Assuming Arrhenius parameters reported in Table S5, we obtain timescales suggesting reequilibration occurs under lunar-relevant conditions (Fig. 5). For plagioclase, the maximum observed half major axis is 3 mm in 60015,113 and 61016,218, and we assume an effective L one third of this maximum reported radius owing to the aspect ratio of plagioclase crystals. Maximum pyroxene radii are 0.5 mm in 62255,3,42 in lunar anorthosite (McGee, 1993). At a T of 1000°C, the time needed to redistribute elements between plagioclase and pyroxenes is less than 200 Myr; diffusive reequilibration is approximately an order of magnitude faster for each 100°C increases in temperature. Given the young ages of many of the ferroan anorthosites (e.g., 4290 ± 85 Ma of sample 62236; Borg et al., 1999) compared to proposed lunar formation times (e.g., 4.425 ± 0.025 Ga; Maurice et al., 2020) and magma ocean solidification timescales (e.g., 150 to 200 Ma; Maurice et al., 2020), these reequilibration timescales are reasonable.

5. Monte-Carlo simulations modeling the formation of lunar anorthosites

5.1. Simulations assuming fixed mineral modes

In order to make a more specific evaluation of the conditions under which subsolidus reequilibration occurs, we ran 100,000

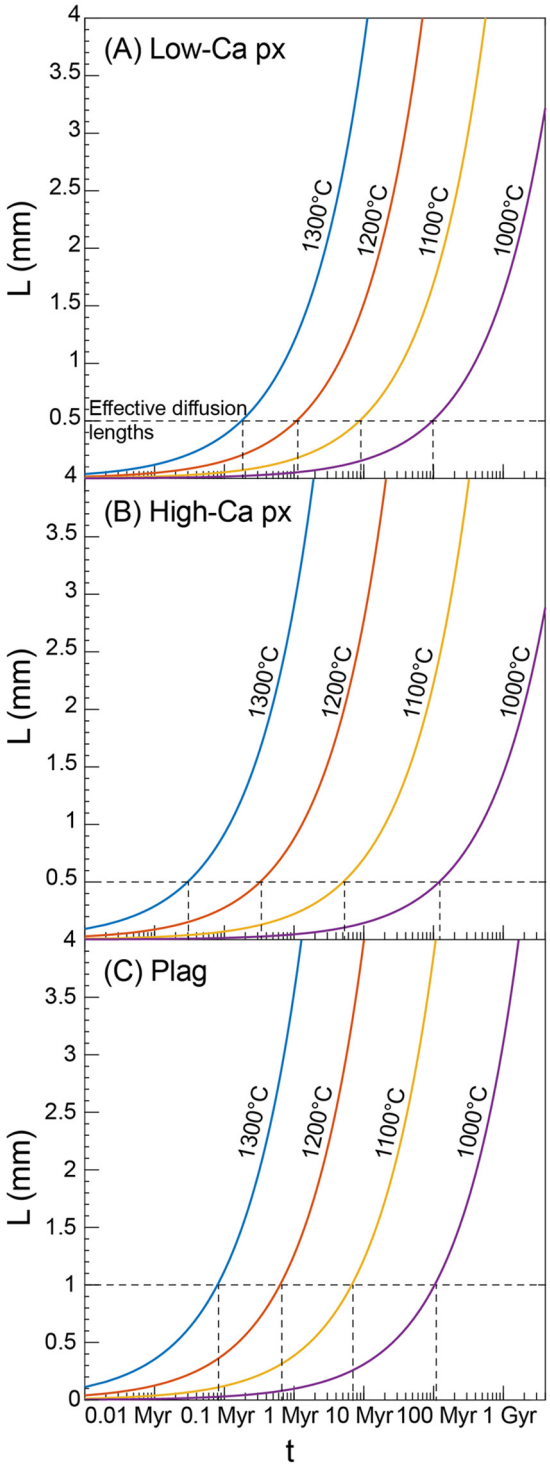

Fig. 5. Diffusive equilibration timescales for plagioclase and pyroxene as a function of effective diffusion length; (**A**) low-Ca pyroxene, (**B**) high-Ca pyroxene and (**C**) plagioclase assuming volume diffusion for different temperatures. L represents the approximate effective diffusion length of a grain reequilibrated at the specified T and time (t) conditions. The horizontal dashed lines show maximum effective diffusion lengths reported for lunar samples. For plagioclase, the maximum observed half major axis is 3 mm in 60015,113 and 61016,218, but according to the typical aspect ratio of plagioclase, the effective L is estimated to be one third of this maximum reported radius. Maximum pyroxene radii are 0.5 mm in 62255,3,42 in lunar anorthosite reported by McGee (1993). Volume diffusion in pyroxene is slower than plagioclase, which may be rate limiting in lunar anorthosites, depending on grain size. Diffusive reequilibration may be expected within timescales less than 200 Myr, even at 1000°C, and is approximately an order of magnitude faster for each 100°C increase in T. See Table S5 for a summary of Arrhenius parameters used in these calculations.

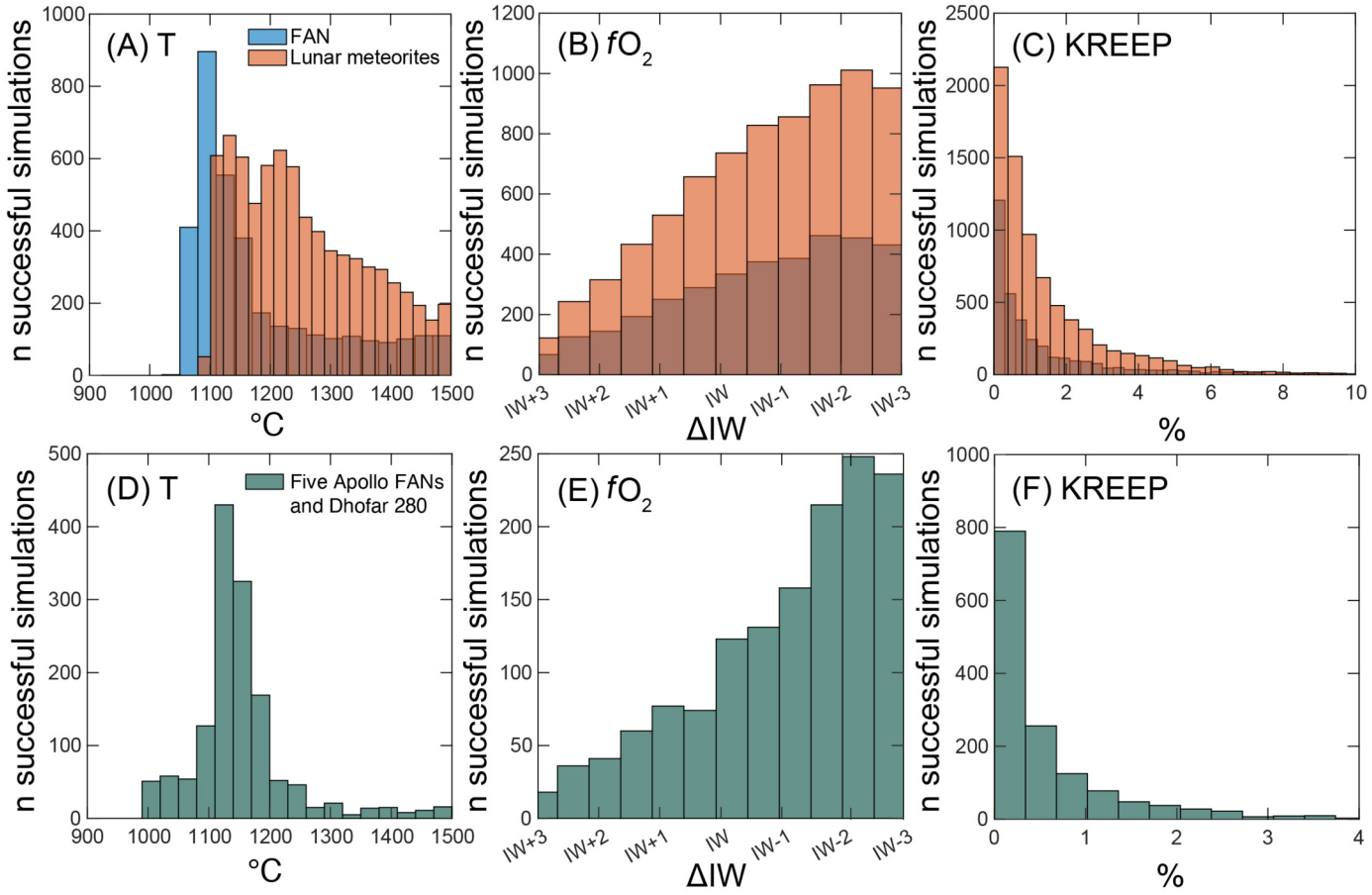

Fig. 6. Histograms showing successful Monte-Carlo simulations testing conditions under which subsolidus reequilibration after minor KREEPy component addition reproduce the compositions of Apollo FANs and lunar anorthositic meteorites. The first row shows simulations assuming fixed mineral modes (95.2% plagioclase + 3.6% low-Ca pyroxene + 1.2% high-Ca pyroxene, (**A**)-(**C**), Table S2) and the second row shows simulations using measured mineral modes (data in Table S2, (**D**)-(**F**)). For simulations with fixed mineral modes (**A**)-(**C**), the models assume the pyroxenes crystallized from the LMO and partition coefficients are calculated using major elements in plagioclase and pyroxene from both FANs (data from McGee, 1993; Papike et al., 1997; Pernet-Fisher et al., 2019) and lunar meteorites (data from Cahill et al., 2004; Roberts et al., 2019; Russell et al., 2014; and Dhofar 280 in this study). For simulations based on reported mineral modes (**D**)-(**F**), the models assume the pyroxenes crystallized from trapped magma ocean liquid within the anorthositic flotation crust. Measured compositions of pyroxenes and plagioclase are used to calculate partition coefficients (Table S2). For all simulations, the crystallization sequence is from Charlier et al. (2018), assuming an LMO with a LPUM bulk major element composition, a slightly depleted trace element bulk composition, and using modeled plagioclase crystallized from 82 to 98 percent solidification of the LMO. The threshold to filter successful simulations for each plagioclase is calculated considering the propagation of errors (Table S3). Most successful simulations assume Ts of 1050-1250 °C, $fO_2 \sim$ IW-2, and less than 1% KREEPy component addition.

simulations per model using a Monte-Carlo approach assuming different temperatures, fO_2 and added KREEPy component proportion to determine which combinations of parameters produce acceptable fits to the lunar samples. In our simulations, we limit T to between 1000 and 1500°C, the fO_2 between IW-3 and IW+3, and the percentage of KREEPy component in anorthosites between 0 and 10%. We test a wide range of parameter combinations in the Monte-Carlo simulations to evaluate whether peaks in the T, fO_2, and the percentage of KREEPy component distribution results are physically reasonable. Though lunar researchers typically invoke low fO_2s (∼IW-1, e.g., Rutherford et al., 2017), recent studies on the fO_2s of specific lunar interior reservoirs suggest the possibility of more oxidized conditions. Guenther et al. (2022) argue the Apollo 17 orange glass source may experience melting at relatively higher fO_2 (∼IW+1.5) based on results of multisaturation experiments. Tartèse et al. (2021) suggested that moderately volatile element depletion of returned lunar samples is consistent with degassing of their source materials in a magma ocean with an fO_2 close to FMQ+2.3.

In our Monte Carlo simulations, we apply the average mineral modes of lunar FANs according to our compilation (95.2% plagioclase + 3.6% low-Ca pyroxene + 1.2% high-Ca pyroxene, Table S1) as well as the average major element concentrations of plagioclase and pyroxenes for both Apollo FANs and lunar anorthositic meteorites (Table S3) to calculate representative partition coefficients. We consider simulations that recover a natural sample within the errors of its Eu/Eu* and $(Ce/Sm)_{CI}$ successful (Table S3). We compare the successful results for plagioclase from Apollo FANs and lunar anorthositic meteorites and find that the slightly depleted initial bulk LMO composition produces the most successful simulations (Figs. 6A-C; 3,431 and 7,753 successful simulations out of 100,000 attempts for FANs and meteorites respectively; for comparison, the number of successful simulations for the moderately depleted bulk composition are 2,722 and 5,656, for the chondritic are 3,136 and 7,404; Fig. S8). Most successful reequilibration temperatures range from 1050 to 1250 °C, fO_2 is ∼IW-2, and the added KREEPy component percentage is less than one. Such high temperature implies the nonnegligible contribution of thermal metamorphism to lunar anorthositic crust (e.g., Pernet-Fisher and Joy, 2022), and conforms to the petrographic description of some FANs (e.g., granulitic texture; McGee, 1993).

The temperature range is consistent with the equilibrium temperatures of lunar granulitic noritic anorthosites suggested by McLeod et al. (2016), 1050 to 1100°C, which also support lunar crustal reworking subsequent to LMO crystallization. We note that the temperatures of successful simulations are ∼100°C higher for

anorthositic meteorites, otherwise, parameter combinations in successful models are similar for FANs and anorthositic meteorites. After considering the propagation of errors, we observe that a bulk Moon with an enriched REE initial trace element bulk LMO composition cannot reproduce natural samples with low $(Ce/Sm)_{CI}$ and high Eu anomalies (Fig. S8D), while other initial bulk trace element compositions successfully reproduce almost all plagioclase, except one from clast H4 in lunar meteorite NWA 10986, which shows the lowest $(Ce/Sm)_{CI}$ of all plagioclase (Roberts et al., 2019; Fig. S8).

We investigated alternatives to the addition of KREEP basalt 15386 prior to subsolidus reequilibration, such as Mg-suite liquid (represented by Apollo samples 15455, 77215). Owing to the relatively lower REE concentrations and small Eu anomaly compared to KREEP basalt, it is necessary to add 8% or even more into anorthosites to achieve the effect similar to that of adding 1% KREEP basalt, which is impossible in practice as introducing so much Mg-suite liquid will produce excessive mafic mineral modes inconsistent with the ferroan anorthosites (Fig. S2). We additionally tested addition of other KREEPy components (e.g., high-K KREEP; Warren, 1989), which did not significantly change the Monte-Carlo simulation results.

Subsolidus reequilibration can reproduce the REE patterns of almost all plagioclase in different subgroups of FANs as subdivided by McGee (1994), assuming Ts between 1050 and 1250°C and fO_2 between IW-1 to IW-2 by adding <1% KREEPy component, with a slightly depleted initial trace element bulk composition (Figs. 7A-D). For sample 67215 which has been classified as a mafic ferroan anorthosite (Floss et al., 1998), we need to add more KREEPy component (but still less than 2%) to reproduce the REE pattern (Fig. 7B). We note the higher K content in plagioclase in 67215 also implies the addition of more KREEPy component (K varies from 148 to 262 ppm, Floss et al., 1998).

5.2. Simulations with reported mineral modes

In the above simulations, the pyroxene modes and compositions assumed (initially in equilibrium with LMO liquids from which they crystallized) impose model dependence. In real lunar samples, both low-Ca pyroxenes and high-Ca pyroxenes exist, but some LMO crystallization models only have one or no crystallization sequence including plagioclase, high-Ca pyroxene and low-Ca pyroxene, limiting the crystallization sequences that we can model. Considering the nonlinear relationship between An in plagioclase and Mg# in coexisting pyroxenes in lunar anorthosites, part or all of pyroxenes could crystallize from trapped liquid (e.g., Jolliff and Haskin, 1995), if we assume they are not magma ocean cumulates (e.g., Dygert et al., 2017; Raedeke and McCallum, 1980; Piskorz and Stevenson, 2014). To reduce model dependence, here we model a smaller number of samples with measured mineral modes. During the subsolidus reequilibration calculations, we use the site parameters for ions in pyroxenes and plagioclase based on measured major element compositions (Table S2) to calculate the partition coefficients and assume all pyroxenes crystallized from trapped magma ocean liquid between plagioclase grains. We ran 100,000 simulations per sample. Despite the small number of samples available owing to data limitations (Apollo FAN 15415, 60025, 60135, 60015, 65325; and lunar meteorite Dhofar 280 in this study; Table S2), the results are similar to those presented assuming fixed mineral modes. Again, parameter combinations in successful models for Apollo FANs are similar to those for lunar anorthositic meteorites. The assumption of a slightly depleted (Figs. 6D-F) initial bulk LMO produces the most successful simulations (1,417 out of 600,000 simulations) among different initial compositions and can reproduce every plagioclase, with subsolidus reequilibration Ts around 1100 °C, fO_2 around IW-2, and the percentage of KREEPy component less than 1% (Figs. 7E-F). A number of the successful simulations utilized plagioclase that crystallized at a relatively late stage of LMO solidification (Figs. S9 and S10), which may be consistent with the asymmetric crustal growth model (Arai et al., 2008; Ohtake et al., 2012).

Simulation results for other bulk trace element LMO compositions and experimentally determined crystallization sequences are shown in Figs. S9 and S10. Different models showed highly similar results in T, fO_2 and the percentage of KREEPy component added. Simulations testing enriched and chondritic bulk LMOs produce fewer successful simulations (64 and 1,302 out of 600,000 simulations, respectively).

5.3. Reconciling a LREE depleted bulk Moon with isotopic characteristics of lunar samples

The number of successful simulations and successful simulation conditions are similar for models assuming a slightly depleted and moderately depleted initial lunar trace element bulk composition (Fig. S9). However, the moderately depleted model has superchondritic Sm/Nd while slightly depleted model has near-chondritic Sm/Nd (Fig. 2A). Isotopic study of urKREEP rich samples (KREEPy Mg-suite rocks and KREEP basalt) has revealed isotopically negative initial ε^{143}Nd (e.g., 15386, 76535, 78238 and NWA 773; Borg et al., 2017, 2009; Edmunson et al., 2009; Gaffney and Borg, 2014), suggesting their KREEPy component originated from an LMO residual liquid with subchondritic Sm/Nd. If the LREE of the initial LMO is too depleted, the late residual liquid produced by LMO crystallization would be LREE depleted and have a superchondritic Sm/Nd (Fig. 2B). Because a slightly depleted pattern has a near chondritic Sm/Nd ratio, the residual liquid in simulations assuming slightly depleted REE abundances is consistent with isotopic variations in natural samples (Fig. 2B). Remelting of cumulates of this residual liquid produces melt with KREEPy REE patterns with KREEPy negative Eu anomalies (Fig. 2C).

Isotopic studies that applied the long and short lived Sm-Nd systems to lunar samples suggest the anorthosites formed from a LREE-depleted source or the initial bulk Moon is LREE-depleted (e.g., Borg et al., 1999; Boyet and Carlson, 2007). Alternatively, measured ^{142}Nd anomalies in meteorites may suggest the Moon accreted from material with a chondritic REE pattern but an enstatite chondrite-like initial ^{142}Nd composition (Boyet et al., 2015), i.e., their apparently depleted ^{142}Nd source reflects nucleosynthetic anomalies. Subsolidus reequilibration of lunar anorthosites following LMO solidification would produce apparently depleted initial sources, but addition of a KREEPy component would make the initial sources apparently more enriched. Thus, depending on the geologic history of each sample, either proposed explanation for apparently depleted initial ^{142}Nd may be consistent with our model.

6. Magmatic evolution after a cumulate mantle overturn event and its significance for geochronology

In the process of LMO crystallization, the olivine and pyroxenes that crystallized in the early LMO are magnesium rich. As LMO solidification progresses, iron and heavy incompatible element abundances (e.g., Ca, Ti) in the magma increase continuously, forming a gravitationally unstable cumulate pile with density increasing upward (Hess and Parmentier, 1995). This unstable density structure may produce gravitationally driven overturn, causing the denser shallower material, especially ilmenite-rich cumulates, to sink into the lunar interior as viscous solids, displacing deep mantle cumulates that rose to the crust-mantle boundary and melted to form the intrusive Mg-suite (Prissel and Gross, 2020). New constraints on the petrogenesis of lunar anorthosites provide an opportunity

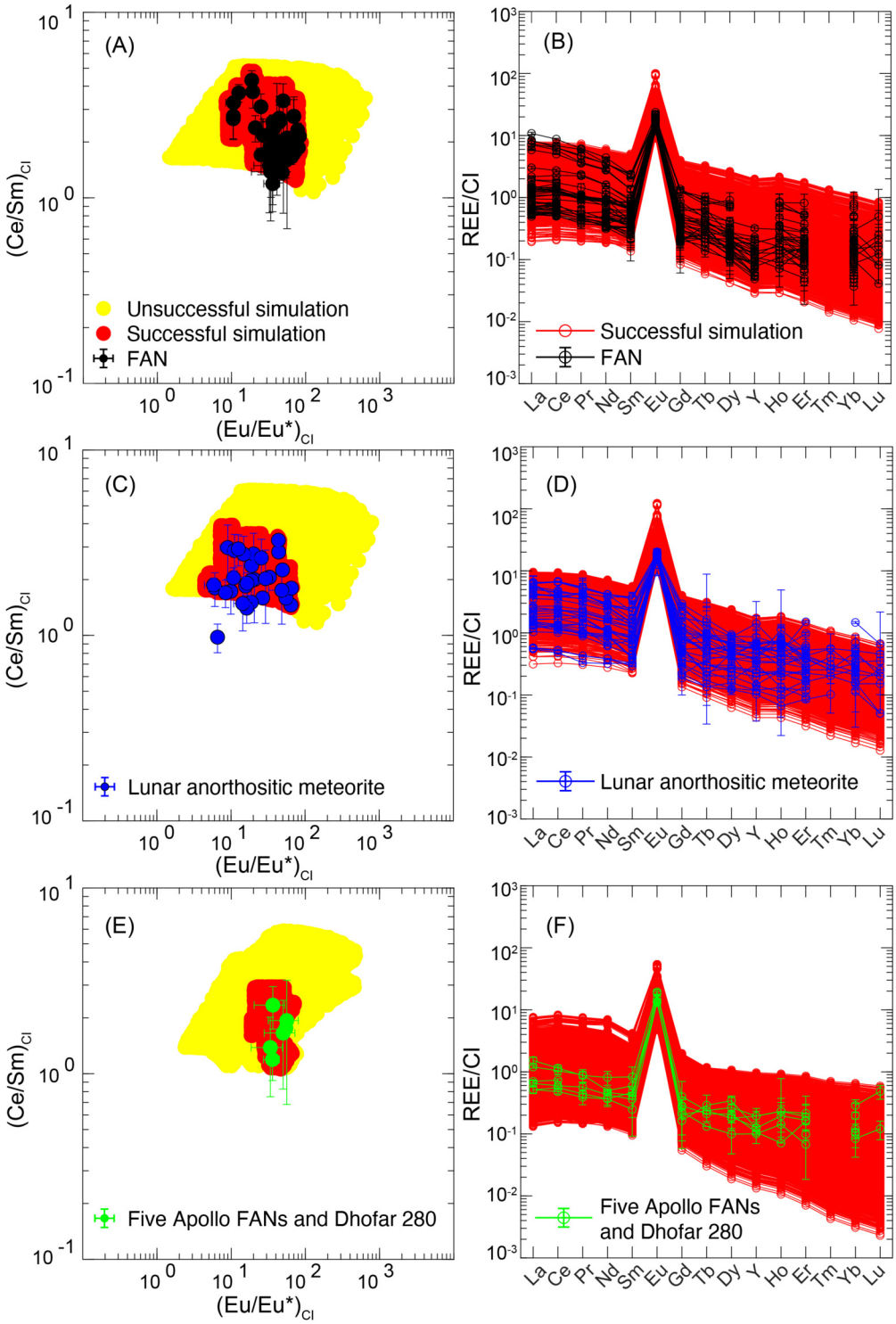

Fig. 7. Successful Monte-Carlo simulation results assuming Ts between 1050 and 1250°C, fO_2 between IW-1 to IW-2, and addition of <2% KREEPy component. (**A**)-(**D**): Simulations assuming fixed mineral modes; (**E**)-(**F**): Simulations assuming reported mineral modes. All simulations assume a slightly depleted initial trace element bulk composition during subsolidus reequilibration. We find that within this combination of parameters almost all the plagioclase can be reproduced, by the standard of Eu/Eu* and $(Ce/Sm)_{CI}$ or the entire REE pattern.

to reevaluate lunar magmatic evolution in the context of mantle overturn. After demonstrating the important role of a KREEPy component and subsolidus reequilibration for the formation of the FANs, we propose a post-LMO model for petrogenesis and secondary magmatic processing of the lunar anorthosites (Fig. 8).

We start with a simplistic physical model that can help us understand the petrogenesis of lunar anorthosites as well as the evolution of the Moon (Fig. 8A). As the deep cumulates migrated upward during cumulate mantle overturn, they experienced decompression melting and brought heat to the crust-mantle boundary, promoting subsolidus reequilibration (Longhi, 2003). At this time, a small amount of KREEPy melt penetrated into the anorthositic crust, promoting and participating in the subsolidus reequilibration. This model restricts most reequilibrated anorthosites to the

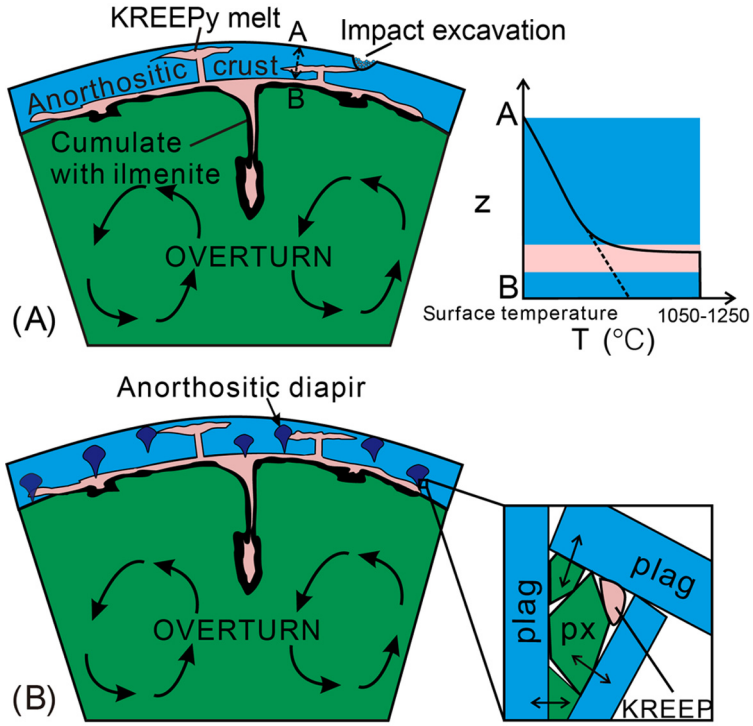

Fig. 8. Schematic illustrations showing two scenarios for the magmatic evolution of the lunar crust after magma ocean solidification and a cumulate mantle overturn event. (**A**) A simple scenario that accounts for the input of a KREEPy component and heat source in the crust. After gravitational overturn, KREEPy components beneath the anorthositic crust intrude into the anorthositic crust. These intruding melts may be the parental magmas of KREEP basalts, Mg-suite and alkali-suite. The KREEPy melts interact with the surrounding anorthosites and provide a heat source to promote subsolidus reequilibration. (**B**) A more complex model invoking upwelling of anorthositic diapirs. In this scenario, the overturn event brings hot material from the lunar interior to the base of the crust, heating anorthosites hybridized by KREEPy melt. Extensive diapirism transports the anorthosites toward the crustal surface while and/or after they reequilibrate. These models reconcile an LMO scenario with the contemporaneous ages of the anorthosites and Mg-suite rocks (see Section 6). The source of the KREEPy melt in these illustrations is schematic, it may originate from heterogeneities in a previously hybridized mantle.

deeper crust (i.e., at or near the crust-mantle boundary), since only in the relatively lower crust, anorthosites contact upwelling, hot mantle materials and mantle melts which would facilitate reequilibration (e.g., Pernet-Fisher and Joy, 2022; Fig. 8A). Without a mechanism for emplacing the deep cumulates in shallower crust, reequilibrated anorthosites would not be sampled unless they were excavated by deep impacts. In addition, elemental redistribution between plagioclase and pyroxene in lunar anorthosites could require hundreds of millions of years for some anorthosites with large grain size as we suggested above. Radiogenic heat production in KREEPy melt beneath the crust would provide a longer-lived heat source, with the magnitude of heat production controlled by heat-producing element (HPE) abundances and the volume of the HPE-rich reservoir. Without a global mechanism to carry enough KREEPy materials into the crust, heat provided by injected magma may not be sufficiently prolonged to produce reequilibration.

In order to address aforementioned weaknesses of the more simplistic model, a second model is proposed (Fig. 8B). In this second scenario, the hot materials originating from the interior of the Moon heat the lower crust, forming a multitude of low-density anorthositic subsolidus diapirs which buoyantly migrate into the upper crust. They are contaminated by KREEPy melt before and/or during upwelling, resulting in extensive high-temperature subsolidus reequilibration. A large number of diapirs are emplaced on or near the lunar surface, burying older crust (Dygert et al., 2017), explaining the universality of moderate Eu anomalies in both Apollo sampled anorthosites and lunar anorthositic meteorites (e.g., Fig. 1B). This model agrees with our Monte-Carlo simulation results that suggest the resurfaced anorthosites were located in the deeper crust before they upwelled, as they precipitated in the last LMO solidification stages (Figs. S8 - S10). Moreover, the time required for subsolidus reequilibration can be satisfied by the radiogenic heat from the KREEP-rich material residing beneath the crust, which is widely injected into the crust through diapirism.

The model we propose here is also supported by geochronological research. Age overlap between ferroan anorthosites (e.g., 4290 ± 85 to 4573 ± 160 Ma; Borg et al., 2015) and the Mg-suite, which intrudes the anorthosites, (e.g., 4283 ± 23 to 4450 ± 270 Ma; Carlson et al., 2014) is perplexing and often considered to be related to post-crystallization metamorphic histories. A traditional LMO crystallization model cannot explain this age overlap because anorthosite is a product of LMO crystallization, while the parental magma of Mg-suite is formed by melting of early LMO cumulates that were hybridized by late LMO crystallization products (e.g., urKREEP and plagioclase; Prissel and Gross, 2020). A similar discordance appears for the lunar KREEPy component, which is the product of very late stage LMO crystallization (solidification equal or higher than 99 percent; Jing et al., 2022) but the model ages for ur-KREEP are 4350 ± 34 Ma (Borg et al., 2015), overlapping with ages of FAN (which crystallizes when the LMO PCS is ~80). The geochronological evidence strongly suggests a globally perturbing thermal event (presumably during a cumulate mantle overturn event) that disrupted the chronometers of anorthosites (Shearer and Papike, 2005). Subsolidus reequilibration and deformation-induced grain size reduction (e.g., Mehl and Hirth, 2008) associated with upwelling of anorthositic diapirs would raise the temperature above the closure temperature of radiogenic isotope chronometers and thus reset the ages, making them consistent with ages of Mg-suite rocks produced in the aftermath of cumulate mantle overturn.

According to remote sensing data, the distribution of a KREEPy signature on the lunar surface presents clear dichotomy with

the nearside being highly enriched compared to the farside (e.g., Lawrence et al., 2000). Plagioclase in lunar anorthositic meteorites (many presumably from the farside highlands; e.g., Korotev et al., 2003) generally have less pronounced Eu anomalies than those in Apollo FANs (e.g., Fig. 3A). To reproduce the compositions of the meteorites, our Monte Carlo simulations require a higher temperature and similar KREEPy component during subsolidus reequilibration compared with the nearside Apollo anorthosites (Fig. 6). This implies that a KREEP signature was globally distributed in the lunar subsurface at the time the crust reequilibrated. The apparent present day hemispheric dichotomy in KREEP reflects bias related to the surface expression of KREEP (perhaps owing to a thicker farside crust, Wieczorek et al., 2013), or suggests hemispheric redistribution of KREEP in the Moon during or subsequent to crustal reequilibration (e.g., Ghods and Arkani-Hamed, 2007; Li et al., 2019), which would have also postdated formation of the South Pole Aitken basin (Lawrence et al., 2000; Moriarty et al., 2021).

7. A depleted bulk Moon

Although the Monte-Carlo simulations cannot exclude the possibility of a chondritic Moon as the initial lunar trace element bulk composition, assuming a LREE depleted initial bulk composition produces more successful simulations and reconciles the trace element and isotopic constraints recorded by other lunar samples as mentioned above. We therefore infer the initial bulk Moon is LREE depleted (e.g., Borg et al., 1999; Boyet and Carlson, 2007). According to traditional models, the origin of the Moon is by accretion of material ejected from the impact between a Mars-sized planetary body (Theia) and proto-Earth, implying that most of Moon's initial composition was inherited from Theia (e.g., Canup, 2004). A multitude of isotopic studies have demonstrated isotopic similarity between the Moon and Earth (e.g., the O, K, Si, W, Ti and ^{53}Mn-^{53}Cr isotopic systems; see Melosh, 2014 and references therein), motivating impact simulations that produce a Moon that accretes from mostly terrestrial material (e.g., Ćuk and Stewart, 2012), or that reequilibrates with Earth in the aftermath of the giant impact (e.g., Lock et al., 2018; Pahlevan and Stevenson, 2007). According to the difference in ^{142}Nd/^{144}Nd ratio between the terrestrial samples and chondrites, it is possible that the proto-Earth is LREE depleted or an initial differentiation on Earth finished before 4.53 Ga (Boyet and Carlson, 2005). A complementary LREE enriched reservoir could be lost during accretion (e.g., Allibert et al., 2021; Bourdon et al., 2008), or hidden in Earth's deep interior (e.g., Boyet and Carlson, 2005). If the bulk Earth is chondritic, the new constraints from LREE signatures in the anorthosites imply that the part of the proto-Earth and/or Theia sampled by the Moon-forming giant impact that produced the lunar magma ocean is LREE depleted, consistent with a pre-giant impact differentiation event.

8. Summary and conclusions

Using a new model for Eu partitioning between plagioclase and melt (Dygert et al., 2020), we calculated the REE concentrations of plagioclase in lunar anorthosite assuming they formed from solidification of a lunar magma ocean (LMO). Comparison to natural samples revealed that under Moon-relevant fO_2s, lunar anorthosites cannot be reproduced by LMO solidification alone. An investigation of processes that could subsequently modify the plagioclase compositions showed that subsolidus reequilibration after the addition of a minor KREEPy component can be successfully invoked to fit the variations in REEs in the natural samples.

We used Monte-Carlo simulations to constrain the lunar trace element bulk composition and the conditions under which lunar anorthosites experienced secondary processing after their initial formation. Our results suggest the lunar ferroan anorthosites evolved in an environment with an fO_2 of ~IW-2 at Ts of 1050 - 1250°C after addition of a <1% KREEPy component. Simulations that best fit the lunar anorthosites assume a lunar magma ocean with a slightly LREE depleted bulk composition, which is also consistent with isotopic evidence from lunar samples.

We propose a post-LMO model to explain the petrogenesis of lunar anorthosites. In our model, plagioclase formed from LMO crystallization and coexisting mafic minerals in anorthosites crystallized from the interstitial tapped liquid and/or from the LMO. Because of the gravitational instability of late LMO cumulates, deep magma ocean cumulates upwelled as a complement to the denser sinking ilmenite-bearing cumulates, introducing heat to the lower crust and promoting the formation of anorthositic diapirs. Some KREEPy melts below the anorthosites ascended into the crust under this Moon-wide agitation, producing subsolidus reequilibration which reconciles the Eu anomalies and REE patterns of the anorthosites, as well as the overlap in ages of Mg-suite, KREEP basalt and ferroan anorthosites.

CRediT authorship contribution statement

D.J.: investigation, visualization, and writing. N.D.: methodology, writing and supervision.

Declaration of competing interest

The authors declare that they have no known competing financial interests or personal relationships that could have appeared to influence the work reported in this paper.

Data availability

All data underlying the study are published and referenced, and/or fully and completely presented in the Supplementary Materials.

Acknowledgements

We thank Yan Liang for helpful discussions, Allan Patchen for his help with electron microprobe analysis, and Soumen Mallick and Brendan Anzures for their assistance with LA-ICP-MS analysis at Brown University. We thank Katherine Joy and Wim van Westrenen for their constructive reviews, Frederic Moynier for efficient editorial handling, and two anonymous reviewers for comments on an earlier version of this manuscript. This work was supported by NASA Solar System Workings award 80NSSC20K0467 to N.D.

Appendix A. Supplementary material

Supplementary material related to this article can be found online at https://doi.org/10.1016/j.epsl.2022.117958.

References

Allibert, L., Charnoz, S., Siebert, J., Jacobson, S.A., Raymond, S.N., 2021. Quantitative estimates of impact induced crustal erosion during accretion and its influence on the Sm/Nd ratio of the Earth. Icarus 363, 114412.

Arai, T., Takeda, H., Yamaguchi, A., Ohtake, M., 2008. A new model of lunar crust: asymmetry in crustal composition and evolution. Earth Planets Space 60, 433–444.

Arevalo, R., McDonough, W.F., 2010. Chemical variations and regional diversity observed in MORB. Chem. Geol. 271, 70–85.

Barford, N.C., 1985. Experimental Measurements: Precision, Error and Truth. Wiley, Chichester.

Binder, A.B., 1974. On the origin of the moon by rotational fission. Moon 11, 53–76.

Borg, L., Norman, M., Nyquist, L., Bogard, D., Snyder, G., Taylor, L., Lindstrom, M., 1999. Isotopic studies of ferroan anorthosite 62236: a young lunar crustal rock from a light rare-earth-element-depleted source. Geochim. Cosmochim. Acta 63, 2679–2691.
Borg, L.E., Gaffney, A.M., Shearer, C.K., DePaolo, D.J., Hutcheon, I.D., Owens, T.L., Ramon, E., Brennecka, G., 2009. Mechanisms for incompatible-element enrichment on the Moon deduced from the lunar basaltic meteorite Northwest Africa 032. Geochim. Cosmochim. Acta 73, 3963–3980.
Borg, L.E., Gaffney, A.M., Shearer, C.K., 2015. A review of lunar chronology revealing a preponderance of 4.34–4.37 Ga ages. Meteorit. Planet. Sci. 50, 715–732.
Borg, L.E., Connelly, J.N., Cassata, W.S., Gaffney, A.M., Bizzarro, M., 2017. Chronologic implications for slow cooling of troctolite 76535 and temporal relationships between the Mg-suite and the ferroan anorthosite suite. Geochim. Cosmochim. Acta 201, 377–391.
Bourdon, B., Touboul, M., Caro, G., Kleine, T., 2008. Early differentiation of the Earth and the Moon. Philos. Trans. R. Soc. Lond. A 366, 4105–4128.
Boyet, M., Carlson, R.W., 2005. 142Nd evidence for early (> 4.53 Ga) global differentiation of the silicate Earth. Science 309, 576–581.
Boyet, M., Carlson, R.W., 2007. A highly depleted moon or a non-magma ocean origin for the lunar crust? Earth Planet. Sci. Lett. 262, 505–516.
Boyet, M., Carlson, R.W., Borg, L.E., Horan, M., 2015. Sm–Nd systematics of lunar ferroan anorthositic suite rocks: constraints on lunar crust formation. Geochim. Cosmochim. Acta 148, 203–218.
Cahill, J.T., Floss, C., Anand, M., Taylor, L.A., Nazarov, M.A., Cohen, B.A., 2004. Petrogenesis of lunar highlands meteorites: Dhofar 025, Dhofar 081, Dar al Gani 262, and Dar al Gani 400. Meteorit. Planet. Sci. 39, 503–529.
Canup, R.M., 2004. Origin of Terrestrial Planets and the Earth–Moon System. Phys. Today 57, 56–62.
Carlson, R.W., Borg, L.E., Gaffney, A.M., Boyet, M., 2014. Rb-Sr, Sm-Nd and Lu-Hf isotope systematics of the lunar Mg-suite: the age of the lunar crust and its relation to the time of Moon formation. Philos. Trans. R. Soc. Lond. A 372, 20130246.
Charlier, B., Grove, T.L., Namur, O., Holtz, F., 2018. Crystallization of the lunar magma ocean and the primordial mantle-crust differentiation of the Moon. Geochim. Cosmochim. Acta 234, 50–69.
Ćuk, M., Stewart, S.T., 2012. Making the Moon from a fast-spinning Earth: a giant impact followed by resonant despinning. Science 338, 1047–1052.
Dygert, N., Liang, Y., Hess, P., 2013. The importance of melt TiO2 in affecting major and trace element partitioning between Fe-Ti oxides and lunar picritic glass melts. Geochim. Cosmochim. Acta 106, 134–151.
Dygert, N., Liang, Y., Sun, C., Hess, P., 2014. An experimental study of trace element partitioning between augite and Fe-rich basalts. Geochim. Cosmochim. Acta 132, 170–186.
Dygert, N., Lin, J.-F., Marshall, E.W., Kono, Y., Gardner, J.E., 2017. A low viscosity lunar magma ocean forms a stratified anorthitic flotation crust with mafic poor and rich units. Geophys. Res. Lett. 44.
Dygert, N., Draper, D.S., Rapp, J.F., Lapen, T.J., Fagan, A.L., Neal, C.R., 2020. Experimental determinations of trace element partitioning between plagioclase, pigeonite, olivine, and lunar basaltic melts and an $fO2$ dependent model for plagioclase-melt Eu partitioning. Geochim. Cosmochim. Acta 279, 258–280.
Edmunson, J., Borg, L., Nyquist, L., Asmerom, Y., 2009. A combined Sm–Nd, Rb–Sr, and U–Pb isotopic study of Mg-suite norite 78238: further evidence for early differentiation of the Moon. Geochim. Cosmochim. Acta 73, 514–527.
Fabbrizio, A., Schmidt, M.W., Petrelli, M., 2021. Effect of fO2 on Eu partitioning between clinopyroxene, orthopyroxene and basaltic melt: development of a Eu3+/Eu2+ oxybarometer. Chem. Geol. 559, 119967.
Floss, C., James, O.B., McGee, J.J., Crozaz, G., 1998. Lunar ferroan anorthosite petrogenesis: Clues from trace element distributions in FAN subgroups. Geochim. Cosmochim. Acta 62, 1255–1283.
Gaffney, A.M., Borg, L.E., 2014. A young solidification age for the lunar magma ocean. Geochim. Cosmochim. Acta 140, 227–240.
Ghods, A., Arkani-Hamed, J., 2007. Impact-induced convection as the main mechanism for formation of lunar mare basalts. J. Geophys. Res., Planets 112.
Gross, J., Joy, K.H., 2016. Evolution, lunar: from magma ocean to crust formation. In: Encyclopedia of Lunar Science, pp. 1–20.
Gross, J., Treiman, A.H., Mercer, C.N., 2014. Lunar feldspathic meteorites: constraints on the geology of the lunar highlands, and the origin of the lunar crust. Earth Planet. Sci. Lett. 388, 318–328.
Guenther, M.E., Krein, S.M.B., Grove, T.L., 2022. The influence of variable oxygen fugacity on the source depths of lunar high-titanium ultramafic glasses. Geochim. Cosmochim. Acta 334, 217–230.
Haskin, L., Lindstrom, M., Salpas, P., 1981. Some observations on compositional characteristics of lunar anorthosites. In: Lunar and Planetary Science Conference, pp. 406–408.
Hess, P.C., Parmentier, E.M., 1995. A model for the thermal and chemical evolution of the Moon's interior: implications for the onset of mare volcanism. Earth Planet. Sci. Lett. 134.
Jing, J.-J., Lin, Y., Knibbe, J.S., van Westrenen, W., 2022. Garnet stability in the deep lunar mantle: constraints on the physics and chemistry of the interior of the Moon. Earth Planet. Sci. Lett. 584, 117491.
Jolliff, B., Haskin, L., 1995. Cogenetic rock fragments from a lunar soil: evidence of a ferroan noritic-anorthosite pluton on the Moon. Geochim. Cosmochim. Acta 59, 2345–2374.
Korotev, R.L., Jolliff, B.L., Zeigler, R.A., Gillis, J.J., Haskin, L.A., 2003. Feldspathic lunar meteorites and their implications for compositional remote sensing of the lunar surface and the composition of the lunar crust. Geochim. Cosmochim. Acta 67, 4895–4923.
Krättli, G., Schmidt, M.W., 2021. Experimental settling, floatation and compaction of plagioclase in basaltic melt and a revision of melt density. Contrib. Mineral. Petrol. 176, 1–27.
Lawrence, D., Feldman, W., Barraclough, B., Binder, A., Elphic, R., Maurice, S., Miller, M., Prettyman, T., 2000. Thorium abundances on the lunar surface. J. Geophys. Res., Planets 105, 20307–20331.
Li, H., Zhang, N., Liang, Y., Wu, B., Dygert, N.J., Huang, J., Parmentier, E., 2019. Lunar cumulate mantle overturn: a model constrained by ilmenite rheology. J. Geophys. Res., Planets 124, 1357–1378.
Lin, Y., Tronche, E.J., Steenstra, E.S., Van Westrenen, W., 2017. Experimental constraints on the solidification of a nominally dry lunar magma ocean. Earth Planet. Sci. Lett. 471, 104–116.
Lock, S.J., Stewart, S.T., Petaev, M.I., Leinhardt, Z., Mace, M.T., Jacobsen, S.B., Cuk, M., 2018. The origin of the Moon within a Terrestrial Synestia. J. Geophys. Res., Planets 123, 910–951.
Lodders, K., 2021. Relative atomic solar system abundances, mass fractions, and atomic masses of the elements and their isotopes, composition of the solar photosphere, and compositions of the major chondritic meteorite groups. Space Sci. Rev. 217, 1–33.
Longhi, J., 1978. Pyroxene stability and the composition of the lunar magma ocean. Proc. Lunar Planet. Sci. Conf., 285–306.
Longhi, J., 2003. A new view of lunar ferroan anorthosites: Postmagma ocean petrogenesis. J. Geophys. Res., Planets 108.
Longhi, J., 2006. Petrogenesis of picritic mare magmas: constraints on the extent of early lunar differentiation. Geochim. Cosmochim. Acta 70, 5919–5934.
Maurice, M., Tosi, N., Schwinger, S., Breuer, D., Kleine, T., 2020. A long-lived magma ocean on a young Moon. Sci. Adv. 6.
McDonough, W.F., Sun, S.-S., 1995. The composition of the Earth. Chem. Geol. 120, 223–253.
McGee, J.J., 1993. Lunar Ferroan Anorthosites - mineralogy, compositional variations, and petrogenesis. J. Geophys. Res., Planets 98, 9089–9105.
McGee, J., 1994. Lunar ferroan anorthosite subgroups. Lunar Planet. Sci. Conf., 875.
McLeod, C.L., Brandon, A.D., Fernandes, V.A., Peslier, A.H., Fritz, J., Lapen, T., Shafer, J.T., Butcher, A.R., Irving, A.J., 2016. Constraints on formation and evolution of the lunar crust from feldspathic granulitic breccias NWA 3163 and 4881. Geochim. Cosmochim. Acta 187, 350–374.
Mehl, L., Hirth, G., 2008. Plagioclase preferred orientation in layered mylonites: evaluation of flow laws for the lower crust. J. Geophys. Res., Solid Earth 113.
Melosh, H., 2014. New approaches to the Moon's isotopic crisis. Philos. Trans. R. Soc. Lond. A 372, 20130168.
Moriarty III, D., Watkins, R., Valencia, S., Kendall, J., Evans, A., Dygert, N., Petro, N., 2021. Evidence for a stratified upper mantle preserved within the South Pole-Aitken basin. J. Geophys. Res., Planets 126, e2020JE006589.
Neal, C., Kramer, G., 2003. The composition of KREEP: a detailed study of KREEP basalt 15386. Lunar Planet. Sci. Conf. 2023.
Norman, M.D., Borg, L.E., Nyquist, L.E., Bogard, D.D., 2003. Chronology, geochemistry, and petrology of a ferroan noritic anorthosite clast from Descartes breccia 67215: clues to the age, origin, structure, and impact history of the lunar crust. Meteorit. Planet. Sci. 38, 645–661.
Nyquist, L., Wiesmann, H., Shih, C., Bansal, B., 1976. 15405 Quartz Monzodiorite: Super KREEP, Interdisciplinary Studies by Imbrium Consortium. Center for Astrophysics Publ, Cambridge, MA, pp. 30–41.
Ohtake, M., Takeda, H., Matsunaga, T., Yokota, Y., Haruyama, J., Morota, T., Yamamoto, S., Ogawa, Y., Hiroi, T., Karouji, Y., 2012. Asymmetric crustal growth on the Moon indicated by primitive farside highland materials. Nat. Geosci. 5, 384–388.
O'Neill, H.S.C., 1991. The origin of the Moon and the early history of the Earth—a chemical model. Part 1: The Moon. Geochim. Cosmochim. Acta 55, 1135–1157.
Pahlevan, K., Stevenson, D.J., 2007. Equilibration in the aftermath of the lunar-forming giant impact. Earth Planet. Sci. Lett. 262, 438–449.
Papike, J.J., Fowler, G.W., Shearer, C.K., 1997. Evolution of the lunar crust: SIMS study of plagioclase from ferroan anorthosites. Geochim. Cosmochim. Acta 61, 2343–2350.
Pernet-Fisher, J.F., Joy, K.H., 2022. Thermal metamorphism on the Moon as recorded by the granulite suite. J. Geol. Soc. 179, jgs2021–jgs2044.
Pernet-Fisher, J., Joy, K., Martin, D., Donaldson Hanna, K., 2017. Assessing the shock state of the lunar highlands: implications for the petrogenesis and chronology of crustal anorthosites. Sci. Rep., Uk 7, 1–12.
Pernet-Fisher, J.F., Deloule, E., Joy, K.H., 2019. Evidence of chemical heterogeneity within lunar anorthosite parental magmas. Geochim. Cosmochim. Acta 266, 109–130.

Phinney, W., 1992. Partition coefficients for iron between plagioclase and basalt as a function of oxygen fugacity: implications for Archean and lunar anorthosites. Geochim. Cosmochim. Acta 56, 1885–1895.
Piskorz, D., Stevenson, D.J., 2014. The formation of pure anorthosite on the Moon. Icarus 239, 238–243.
Prissel, T.C., Gross, J., 2020. On the petrogenesis of lunar troctolites: new insights into cumulate mantle overturn & mantle exposures in impact basins. Earth Planet. Sci. Lett. 551, 116531.
Prowatke, S., Klemme, S., 2006. Trace element partitioning between apatite and silicate melts. Geochim. Cosmochim. Acta 70, 4513–4527.
Raedeke, L.D., McCallum, I., 1980. A comparison of fractionation trends in the lunar crust and the Stillwater Complex. In: Proceedings of the Conference on the Lunar Highlands Crust. Pergamon Press, pp. 133–153.
Rapp, J.F., Draper, D.S., 2018. Fractional crystallization of the lunar magma ocean: updating the dominant paradigm. Meteorit. Planet. Sci. 53, 1452–1455.
Roberts, S.E., McCanta, M.C., Jean, M.M., Taylor, L.A., 2019. New lunar meteorite NWA 10986: a mingled impact melt breccia from the highlands-a complete cross section of the lunar crust. Meteorit. Planet. Sci. 54, 3018–3035.
Rudnick, R., Gao, S., 2014. Composition of the continental crust. Crust, 47.
Russell, S.S., Joy, K.H., Jeffries, T.E., Consolmagno, G.J., Kearsley, A., 2014. Heterogeneity in lunar anorthosite meteorites: implications for the lunar magma ocean model. Philos. Trans. R. Soc. Lond. A 372.
Rutherford, M.J., Head, J.W., Saal, A.E., Hauri, E., Wilson, L., 2017. Model for the origin, ascent, and eruption of lunar picritic magmas. Am. Mineralog., J. Earth Planet. Mater. 102, 2045–2053.
Schmidt, M.W., Kraettli, G., 2022. Experimental crystallization of the lunar magma ocean, initial selenotherm and density stratification, and implications for crust formation, overturn and the bulk silicate Moon composition. J. Geophys. Res., Planets e2022JE007187.
Shearer, C.K., Papike, J., 2005. Early crustal building processes on the moon: models for the petrogenesis of the magnesian suite. Geochim. Cosmochim. Acta 69, 3445–3461.
Snyder, G., Taylor, L., Crozaz, G., 1992b. Zircon/melt partition coefficients for the rare-earth elements in evolved rocks: the usefulness of accessory minerals in petrogenetic studies on the Earth and Moon. Lunar Planet. Sci. Conf.
Snyder, G.A., Taylor, L.A., Neal, C.R., 1992a. A chemical model for generating the sources of mare basalts: combined equilibrium and fractional crystallization of the lunar magmasphere. Geochim. Cosmochim. Acta 56, 3809–3823.
Sun, C.G., Liang, Y., 2013a. The importance of crystal chemistry on REE partitioning between mantle minerals (garnet, clinopyroxene, orthopyroxene, and olivine) and basaltic melts. Chem. Geol. 358, 23–36.
Sun, C.G., Liang, Y., 2013b. Distribution of REE and HFSE between low-Ca pyroxene and lunar picritic melts around multiple saturation points. Geochim. Cosmochim. Acta 119, 340–358.
Sun, C.G., Liang, Y., 2014. An assessment of subsolidus re-equilibration on REE distribution among mantle minerals olivine, orthopyroxene, clinopyroxene, and garnet in peridotites. Chem. Geol. 372, 80–91.
Sun, C.G., Graff, M., Liang, Y., 2017. Trace element partitioning between plagioclase and silicate melt: the importance of temperature and plagioclase composition, with implications for terrestrial and lunar magmatism. Geochim. Cosmochim. Acta 206, 273–295.
Tartèse, R., Sossi, P.A., Moynier, F., 2021. Conditions and extent of volatile loss from the Moon during formation of the Procellarum basin. Proc. Natl. Acad. Sci. 118, e2023023118.
Taylor, S.R., 1982. Planetary Science: A Lunar Perspective. Lunar and Planetary Institute, Houston, p. 502.
Taylor, G.J., Wieczorek, M.A., 2014. Lunar bulk chemical composition: a post-gravity recovery and interior laboratory reassessment. Philos. Trans. R. Soc. Lond. A 372, 20130242.
Torcivia, M.A., Neal, C.R., 2022. Unraveling the components within Apollo 16 ferroan anorthosite suite cataclastic anorthosite sample 60025: implications for the lunar magma ocean model. JGR Planets. https://doi.org/10.1029/2020JE006799.
Treiman, A.H., Maloy, A.K., Shearer, C.K., Gross, J., 2010. Magnesian anorthositic granulites in lunar meteorites Allan Hills A81005 and Dhofar 309: geochemistry and global significance. Meteorit. Planet. Sci. 45, 163–180.
Warren, P.H., 1989. KREEP: major-element diversity, trace-element uniformity (almost). In: Workshop on Moon in Transition: Apollo 14, KREEP, and Evolved Lunar Rocks, pp. 149–153.
Warren, P.H., 1990. Lunar anorthosites and the magma-ocean plagioclase-flotation hypotheses: importance of FeO enrichment in the parent magma. Am. Mineral. 75, 46–58.
Wieczorek, M.A., Neumann, G.A., Nimmo, F., Kiefer, W.S., Taylor, G.J., Melosh, H.J., Phillips, R.J., Solomon, S.C., Andrews-Hanna, J.C., Asmar, S.W., 2013. The crust of the Moon as seen by GRAIL. Science 339, 671–675.
Workman, R.K., Hart, S.R., 2005. Major and trace element composition of the depleted MORB mantle (DMM). Earth Planet. Sci. Lett. 231, 53–72.